Pilz, M., Parolai, S., Stupazzini, M., Paolucci, R., Zschau, J. (2011): Modelling basin effects on earthquake ground motion in the Santiago de Chile basin by a spectral element code. - Geophysical Journal International, 187, 2, pp. 929—945.

DOI: http://doi.org/10.1111/j.1365-246X.2011.05183.x

Geophysical Journal International

Geophys. J. Int. (2011) **187,** 929–945 doi: 10.1111/j.1365-246X.2011.05183.x

Modelling basin effects on earthquake ground motion in the Santiago de Chile basin by a spectral element code

Marco Pilz,[1,2] Stefano Parolai,[3] Marco Stupazzini,[4] Roberto Paolucci[5] and Jochen Zschau[6]

[1] *Helmholtzzentrum Potsdam, German Research Center for Geosciences, Helmholtzstr.* 7, 14467 *Potsdam, Germany. E-mail: pilz@gfz-potsdam.de*
[2] *Universität Potsdam, Institut für Erd- und Umweltwissenschaften, Karl-Liebknecht-Str.* 24, 14476 *Potsdam, Germany*
[3] *Helmholtzzentrum Potsdam, German Research Center for Geosciences, Helmholtzstr.* 7, 14467 *Potsdam, Germany*
[4] *Münchener Rückversicherungsgesellschaft, CU GeoRisks, Königinstr.* 107, 80802 *München, Germany*
[5] *Politecnico di Milano, Dipartimento di Ingegneria Strutturale, Piazza Leonardo da Vinci* 32, 20133 *Milan, Italy*
[6] *Helmholtzzentrum Potsdam, German Research Center for Geosciences, Helmholtzstr.* 7, 14467 *Potsdam, Germany*

Accepted 2011 August 3. Received 2011 August 3; in original form 2011 March 10

SUMMARY

Simulations of strong ground motion within the Santiago de Chile Metropolitan area were carried out by means of 3-D deterministic wave propagation tool based on the spectral element method. The simulated events take into account the pronounced interface between the low-velocity sedimentary basin and the bedrock as well as topography of the area. To verify our model we simulated a regional earthquake recorded by a dense network installed in the city of Santiago for recording aftershock activity after the 2010 February 27 Maule main shock. The results proof the alluvial basin amplification effects and show a strong dependence of spectral amplification in the basin on the local site conditions. Moreover, we studied the seismic response due to a hypothetical $M_w = 6.0$ event occurring along the active San Ramón Fault, which is crossing the eastern edge of the city. The scenario earthquakes exhibit that an unfavourable interaction between fault rupture, radiation mechanism and complex geological and topographic conditions in the near-field region may give rise to large values of peak ground velocity in the basin. Finally, 3-D numerical predictions of ground motion are compared with the one computed according to ground motion prediction equations selected among the next generation attenuation relationships, in terms of ground motion peak values and spectral acceleration. The comparison underlines that the 3-D scenario simulations predict a significantly higher level of ground motion in the Santiago basin, especially over deep alluvial deposits. Moreover, also the location of the rupture nucleation largely influences the observed shaking pattern.

Key words: Earthquake ground motions; Site effects; Wave propagation; South America.

1 INTRODUCTION

The area of Great Santiago in Chile with now over six million inhabitants is one of the most densely populated metropolitan areas in Latin America, with its population having multiplied more than 20-fold during the 20th and the 21st century. Within this period, five earthquakes have caused significant economic losses in the city of Santiago de Chile ($M = 8.2$ on 1906 August 17; $M = 7.8$ on 1936 January 25; $M = 7.4$ on 1965 March 28; $M = 7.8$ on 1985 March 3; $M = 8.8$ on 2010 February 27), with distance from the fault rupture ranging from 80 to 300 km. Not only the occurrence of such distant thrust events represents a latent danger but, moreover, recent studies also suggest that west-verging structures at the western flank of the Andes, parallel to the subduction zone, could trigger earthquakes causing important shaking throughout the alluvial basin and the city (Armijo *et al.* 2010). Therefore, the accurate prediction of ground motion represents a necessary tool for seismic hazard assessment allowing an accurate design of new buildings and a better planning of the retrofitting priority, aiming at mitigating the losses that might occur during future earthquakes.

The situation is exacerbated due to the location of the city of Santiago de Chile in a narrow basin between the Andes and the coastal mountains filled with soft sediments that may strongly modify the seismic ground motion on a small scale. The basin is around 80 km long, 40 km wide, and mainly aligned in north–south direction. It originated from the depression caused by tectonic movements during the Tertiary of an area between two major faults running parallel to the two mountain chains (Fig. 1).

The surface geology of the Santiago basin consists of several different materials (Valenzuela 1978): most of the central and

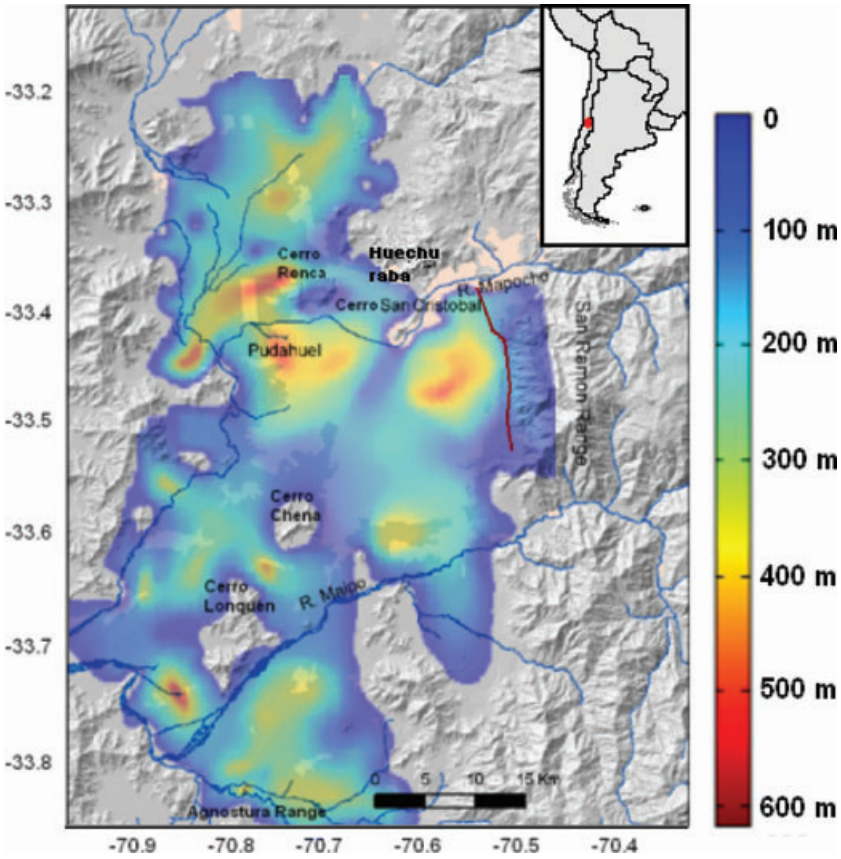

Figure 1. Basin of Santiago de Chile. Locations mentioned in the text are indicated. The red line in the east represents the San Ramón Fault. The thickness of the sedimentary cover as determined by interpolation of gravimetric data is highlighted (Araneda *et al.* 2000). Areas of high housing density are shown in red or in light colours, respectively.

northeastern parts of the city are located on fluvial gravel deposits with a high density and a low deformability. Alluvial silt and high plasticity clay soils deposits make up most of the northwestern part of the basin, with a transition zone existing between these two areas. In the western part of the investigated area (Pudahuel district, see Fig. 1) a layer of ash is known to be at the top of the sedimentary column.

The basement of the Santiago basin is believed to result from volcanic activity aged between the higher Oligocene to the lower Miocene. Its shape is known only indirectly from gravimetric measurements (Araneda *et al.* 2000) and corresponds to an uneven surface that conceals some hill islands that locally outcrop within the basin. The almost linear alignment of some of these hills, such as that for Cerro San Cristóbal, Cerro Chena and Cerro Lonquén (see Fig. 1), may even hint that there might have been a structural control.

2 NUMERICAL SIMULATIONS

In recent years, simulations of earthquake ground motion using realistic velocity structures have seen a rapid advancement. The adopted numerical methods range finite differences (e.g. Olsen *et al.* 1995, Moczo *et al.* 2002, Graves & Wald 2004, Hartzell *et al.* 2006, Harmsen *et al.* 2008) or finite elements (e.g. Bao *et al.* 1998, Aagaard *et al.* 2001, Bielak *et al.* 2005) to discontinuous Galerkin (e.g. Reed & Hill 1973, Arnold 1982, Falk & Richter 1999, Hu *et al.* 1999, Cockburn *et al.* 2000, Giraldo *et al.* 2002, Rivière & Wheeler 2003, Käser & Dumbser 2006, Dumbser & Käser 2006) or spectral elements (SEM). The SEM originally dates back to computational fluid dynamics (Patera 1984) but has further been successfully adapted for addressing problems in seismic wave propagation. Early works on the SEM on seismic wave propagation phenomena by means of Legendre basis functions include Cohen *et al.* (1993), Komatitsch (1997), Faccioli *et al.* (1997), Komatitsch & Vilotte (1998) and Komatitsch *et al.* (1999), whereas Seriani & Priolo (1994), Priolo *et al.* (1994) and Seriani *et al.* (1995) use SEM involving Chebyshev basis functions and a non-diagonal mass matrix.

In general, all these techniques are able to simulate earthquake ground motion with their advantages and disadvantages depending on the specific application (Chaljub *et al.* 2010). In the near-fault region, ground motion is controlled primarily by the source radiation, the rupture propagation characteristics (i.e. slip pattern along the fault), and the complex interaction with the shallow and deep soil deposits. Therefore, particular attention has to be paid when taking into account the surface topography and the sedimentary basin mechanical properties. The influence of the alluvial basin soft soil deposit on seismic wave propagation have been largely illustrated through empirical observations (e.g. Kagawa *et al.* 1992, Kinoshita *et al.* 1992, Phillips *et al.* 1993, Frankel 1994, Chávez-García & Bard 1994, Hatayama *et al.* 1995, Field 1996, Bindi *et al.* 2009) and numerical studies (e.g. Horike *et al.* 1990, Graves 1993, Hisada *et al.* 1993, Moczo *et al.* 1999, Frankel *et al.* 2001, Hartzell *et al.* 2006, Olsen *et al.* 2006, Lee *et al.* 2008a).

To accommodate the surface topography and the complex geometry of the sediment bedrock interface in the Santiago metropolitan

area, which will significantly influence ground motion on a local scale, we carried out numerical simulations making use of the SEM based software package GeoELSE (Stupazzini *et al.* 2009). In the SEM, the description of the geometry of the geological interfaces is a critical task to achieve accurate simulated results and avoiding numerical artefacts due to inappropriate model discretization (i.e. badly dimensioned or highly deformed elements). For the Santiago basin the complex geometry of the sedimentary layers and the sharp transitions between the sediments and underlying bedrock poses a formidable challenge in the discretization of the computational domain. This task was successfully solved by means of the software CUBIT (Blacker *et al.* 1994, White *et al.* 1995, Mitchell 1996) which incorporates a set of advanced meshing schemes specifically developed to handle the hexahedral unstructured meshing problem required when using the SEM. Further recent advances in hexahedral meshing and software optimization are reported by Peter *et al.* (2011).

Moreover, to assess the accuracy of our model and to explain the particular damage pattern in the city of Santiago de Chile, an excellent opportunity is offered by the 2010 February 27 Maule earthquake whose aftershocks have been recorded by a dense temporary seismic network which had been installed in the urban area. With the purpose of verifying our model, we decided first to simulate an observed aftershock since the agreement between recorded and numerically calculated earthquake motion can be considered an ultimate criterion for capability to simulate earthquake ground motion (Chaljub *et al.* 2010).

Therefore, we will first describe the generation of our Santiago basin model and test its quality against an observed aftershock both in the time and frequency domains. The analysis of the aftershock can further provide an adequate explanation of the particular damage pattern in the city. Moreover, we analyse the seismic hazard for the city of Santiago, induced by an event located along the nearby San Ramón Fault, and quantify the influence of basin and topographic effects. According to recent studies, the San Ramón Fault is capable of triggering events up to a moment magnitude of 7.4 (Armijo *et al.* 2010). Finally, a further comparison between our scenarios and the one computed according to ground motion prediction equations (GMPE) selected among the next generation attenuation relationship (NGA) in terms of peak ground motion and spectral acceleration parameters is carried out.

3 SANTIAGO BASIN MODEL AND MESH IMPLEMENTATION

For the simulation of wave propagation the surrounding topography of the large-scale numerical model is constructed based on the GTOPO30 data set, a 30 arcsec digital elevation model (DEM). In addition, for the Santiago metropolitan area the DEM is available with a resolution of 30 m, and the shape of the sediment bedrock interface is provided thanks to dense grid of gravimetric measurements (Araneda *et al.* 2000).

In our model the sedimentary basin mechanical properties are assumed to vary only with depth according v_s (m s^{-1}) = 400 + 55 $z^{1/2}$ with z measured in metres. This relation was found to allow the best fit of the numerical model to a high-resolution model of the *S*-wave velocity of the Santiago basin, which has recently been proposed by Pilz *et al.* (2010). For the *P*-wave velocity we assumed, consistently with Kitsunezaki *et al.* (1990), v_p (m s^{-1}) = 1730 + 60 $z^{1/2}$. The depth dependency of the density is taken from Bravo (1992): ρ (kg m^{-3}) = 2100 + 0.15 z. Inside the sedimentary basin, the smooth vertical variation is taken into account, assigning each Legendre-Gauss-Lobatto point the mechanical properties evaluated according to the prescribed depth variation (Casarotti *et al.* 2007).

The viscoelastic behaviour implemented in GeoELSE is imposed by a modification of the equation of motion. To this purpose, the acceleration term $\rho\frac{\partial^2 u}{\partial t^2}$ of the wave equation is replaced by $\rho(\frac{\partial^2 u}{\partial t^2} + 2\gamma\frac{\partial u}{\partial t} + \gamma^2 u)$, with u being the generic displacement component, ρ being the density and γ the attenuation parameter. It can be shown (Kosloff & Kosloff 1986) that, with such replacement, all frequency components are equally attenuated, resulting in a frequency proportional quality factor $Q = Q_0\frac{f}{f_0}$. The reference frequency f_0, being representative of the frequency range to be propagated, was set equal to 0.5 Hz in this study. Relative to a constant Q model, energy for frequencies greater than f_0 will be underattenuated whereas frequencies smaller than f_0 will be slightly over-damped. However, when f is near f_0, the approximation to a constant Q works well (Graves 1996).

The bedrock is assumed as a cake-layered structure with v_p = 4700 m s^{-1} and v_s = 2400 m s^{-1} between 0 and 2.2 km depth, v_p = 5900 m s^{-1} and v_s = 3200 m s^{-1} between 2.2 and 8.9 km depth, and v_p = 6200 m s^{-1} and v_s = 3450 m s^{-1} below 8.9 km depth (Godoy *et al.* 1999, Barrientos *et al.* 2004).

The final mesh is depicted in Fig. 2 and consists of 1 844 014 elements, the size of which ranges from a minimum of about 60 m (inside the sedimentary basin) up to 900 m. In spite of complex material interfaces, for resolving the wavefield for the shortest period, the number of grid points per wavelength should be at least equal to five. Therefore, the mesh is designed to propagate frequencies up to 1.3 Hz with spectral degree 3 (51 632 392 nodes) and up to around 1.8 Hz with spectral degree 4 (119 860 910 nodes).

The first numerical calculation refers to the simulation of an aftershock occurring on 2010 April 1 at 12:53:07 UTC. This event (M = 5.2) was located around 180 km southwest of the city (latitude 34.65° S, longitude 71.82° W) at a depth of around 11.8 km (USGS NEIC catalogue).

The fault plane for selected event is geometrically defined by a 4.7 km × 3.5 km rectangle, according to Wells & Coppersmith (1994). The rupture is in plane with a constant slip density. The parameters of the source mechanism (strike = 195°, dip = 58°, rake = –142°) are taken from the CMT catalogue. The rupture is assumed to propagate circularly from the hypocentre located in the centre of the rectangle with a rupture velocity of v = 2800 m s^{-1}. The time dependency of the seismic moment tensor source is described by an approximate Heaviside function, that is,

$$M_0(t) = \frac{1}{2}\left[1 + \mathrm{erf}\left(2\frac{t-2\tau}{\frac{\tau}{2}}\right)\right], \quad (1)$$

where erf (...) is the error function and τ is the rise time, measured as the time necessary to attain 5 to 95 per cent of the final slip (Mai 2009). For the simulation of the aftershock the values are selected in such a way that the slip velocity is constant and around 1 m s^{-1}.

4 SIMULATION OF THE 2010 APRIL 1 AFTERSHOCK

A comparison of the velocity waveforms recorded at and simulated for ten sites of the seismic network, that had been installed in the city of Santiago after 2010 March 18, is shown in Fig. 3. All waveforms have been bandpass filtered (0.05 Hz < f < 1.8 Hz). For the analysis non-linear effects were neglected, since ground strains induced by

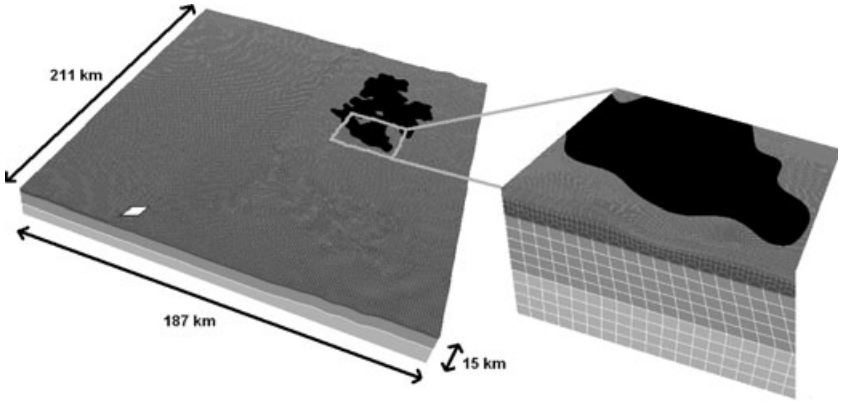

Figure 2. Left-hand side: 3-D hexahedral spectral element mesh adopted for the computation of the 2010 April 1 aftershock with the GeoELSE software. For simplicity, the spectral elements are shown without the Legendre-Gauss-Lobatto nodes. Different colours refer to different mechanical properties. The shape of the Santiago basin is shown in black. The location of the fault is represented by a white rectangle. Right-hand side: Detailed view of the sedimentary basin mesh. The size of the mesh elements is tripled three times to reduce the numerical cost of the simulations by reducing the number of spectral elements and to allow for a larger time step in the explicit conditionally stable time scheme.

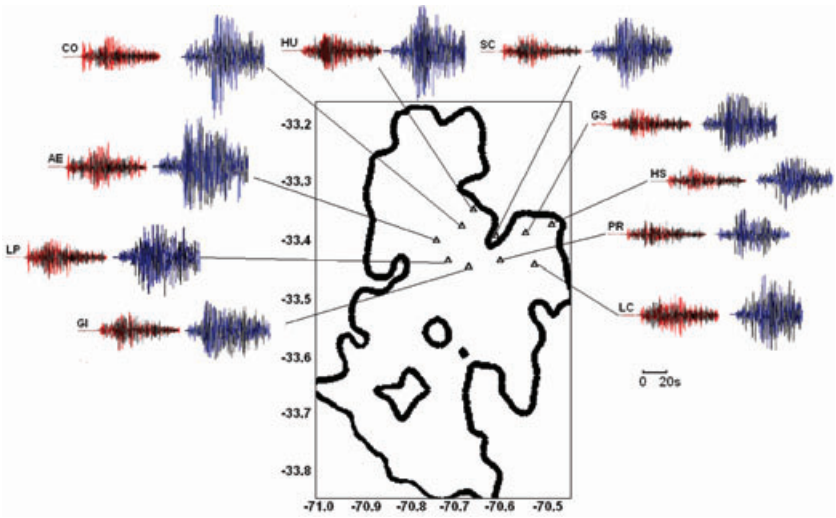

Figure 3. Comparison of recorded vertical (red), recorded radial (blue) and simulated (black) component velocity waveforms of the 2010 April 1 aftershock for ten sites of the network installed in the urban area of Santiago de Chile. The thick black line marks the border between the sedimentary basin and outcropping bedrock. The velocity waveforms are bandpass filtered between 0.05 and 1.8 Hz.

the moderate shaking are relatively small due to large source to site distances.

At first glance, the recorded data can fit reasonably well both on the horizontal and the vertical components in terms of maximum amplitude and duration of the signal. The stations in the northwestern part of the studied area lying on the top of thick sediments (i.e. stations AE, CO, HU and LP) show higher amplitudes and longer shaking durations. On the contrary, for stations located in the central and the eastern part of the study area (GI, GS, HS and PR) smaller amplitudes are found.

When comparing the waveforms, also significant differences and a clear lengthening of ground shaking for some sites of the network can be observed, despite their proximity. We calculate the duration of the event by ignoring the first and the last 5 per cent of the velocity square integral and considering the remaining 90 per cent as the significant contribution (Trifunac & Brady 1975). Several other definitions of earthquake durations can be found in a review by Bommer & Martínez-Pereira (1999).

For each station the duration was divided by the corresponding duration recorded at the reference stations SC. A comparison of the duration ratios of the recordings and simulations is shown in Table 1. As can be seen, the duration of ground shaking is increased for most of the basin sites, in particular for sites in the northern and western part of the basin. For most of the sites, the duration ratios of the simulated and the recorded waveforms match quite well although

Table 1. Duration ratios for stations located in the basin relative to the duration at the reference station SC.

Station	Recording	Simulation
AE	1.56	1.48
PR	1.19	1.25
GI	1.10	1.04
LC	1.40	1.36
GS	1.14	1.04
LP	1.12	1.05
CO	1.30	1.08
HS	0.95	0.89
HU	1.38	1.44

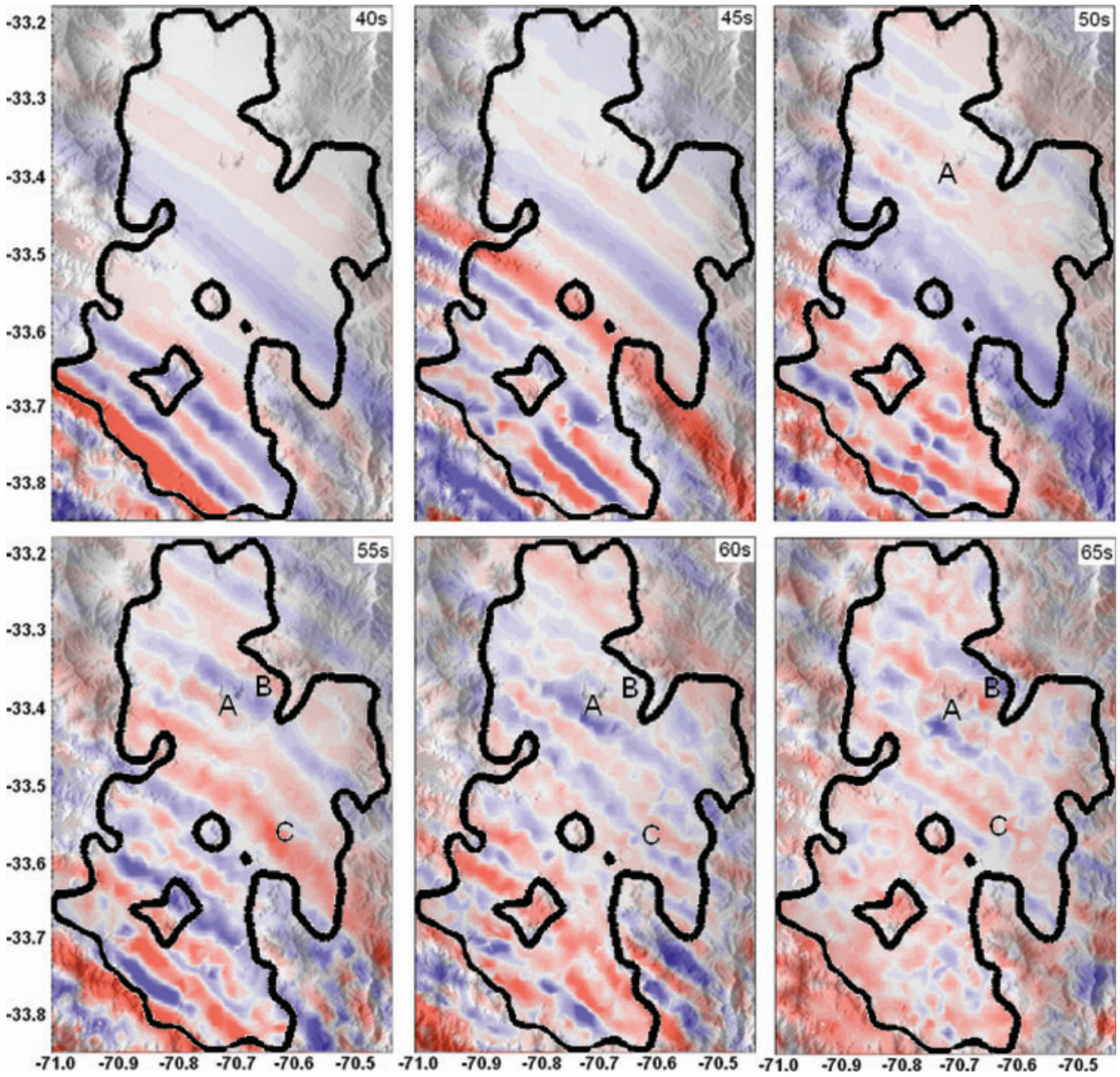

Figure 4. Snapshots of the vertical component of the simulation of the 2010 April 1 earthquake. Red colours indicate positive velocities, and blue colours indicate negative velocities. The position of Cerro Renca is indicated by letter A, Huechuraba district is represented by letter B. The black line indicates the edge of the Santiago basin. The waveforms are clearly distorted and amplified due to topographic and basin effects as also indicated by letter C. See text for further discussion.

there is a slight tendency in the simulations of underestimating the duration ratios.

Aftershock simulation snapshots for the vertical component of the velocity wavefield (bandpass filtered between 0.05 and 1.8 Hz) are shown in Fig. 4. At approximately 25 s the *P*-wave reaches the southwestern edge of the basin with relative small amplitude. The slower but significantly stronger *S*-wave reaches the edge of the basin after around 35 s and propagates further with significantly varying amplitude.

As can be seen, in particular the northwestern part of the basin suffers from very complex ground motion. The Cerro Renca (indicated with letter A in Fig. 4), a hill rising more than 200 m above the surrounding plane, causes the seismic waves to be largely reflected and scattered, especially after 55 s. To the east of Cerro Renca and to the west of Cerro San Cristóbal strong ground motion occurs which might be due to constructive interference between different arrivals reflected at the facing hills (Huechuraba district, labelled B in Fig. 4). In particular, widespread structural damage was found for this part of the city following the 2010 Maule earthquake. Many (in general reinforced concrete) buildings have been partially and seven of them structurally damaged (Bray & Frost 2010, Pilz *et al.* 2011). Also Pilz *et al.* (2009) found quite high amplitudes of the noise H/V spectral ratios in their experimental study and fundamental resonance frequencies of the soil between 0.5 and 3 Hz for that area. This frequency range is likely to be consistent with the structural resonant periods of the damaged structures, most of them having five to ten floors. Hence, a combination of trapping and focusing of seismic energy, combined with resonance effects and insufficient confinement in the bearing walls of these structures (Elnashai *et al.* 2010) might have caused the high impact of the main shock in this part of the Santiago basin.

Interference and amplification effects are also clearly visible in the southwest of the basin between Cerro Chena and Cerro Lonquén (for the exact location of these hills see Fig. 1) between 50 and

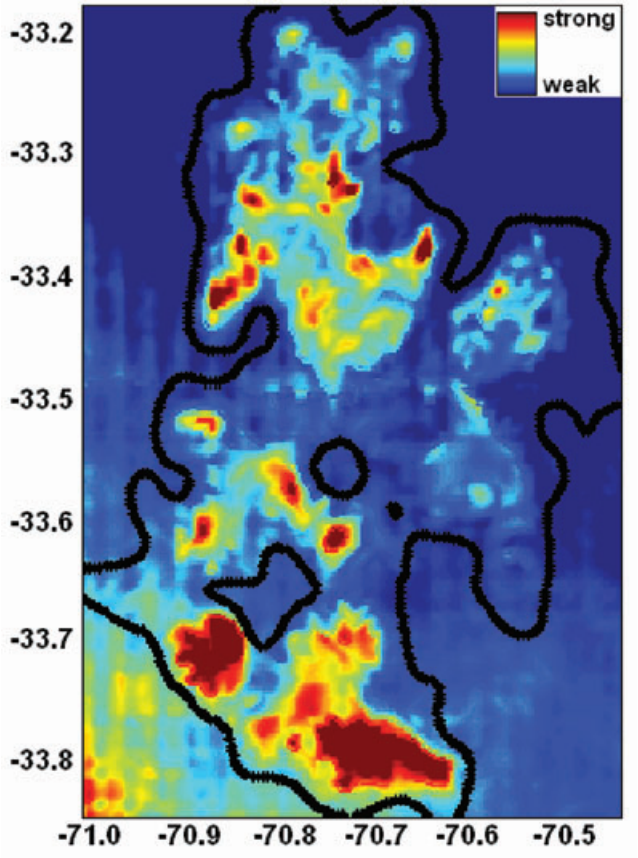

Figure 5. Cumulative kinetic energy calculated after Lee *et al.* (2008b) for the simulation of the 2010 April 1 earthquake. The black line marks the border between the sedimentary basin and outcropping bedrock.

60 s. After around 60 s the main body wave phases have propagated out of the basin; however, large ground velocities still persist in the basin. In particular, the continuation of strong ground shaking is observed above the deepest parts of the basin (especially to the west and southwest of the label A and around label C in Fig. 4, see also Fig. 1).

To further point out the influence of the basin we consider another parameter, the cumulative kinetic energy E_k. This parameter is obtained by summing the square of the velocity amplitude of all three components in the seismogram in time, multiplying the density ρ, then dividing by 2,

$$E_k = \frac{1}{2}\rho(x, y) \int \dot{u}_k^2(x, y, t)\mathrm{d}t. \quad (2)$$

Olsen *et al.* (1995, 1996) found that the cumulative kinetic energy is more closely related to the shaking damage potential since it reflects both the amplitude as well as the duration time of the total motion. The distribution of E_k in the Santiago basin is shown in Fig. 5. Large values especially appear in the southern and northwestern parts of the basin. When comparing with Fig. 1, it seems obvious that most of the energy is trapped where the basin is deepest and the sedimentary cover is thickest. Also the area around Cerro Renca shows large E_k values due to energy that propagates around the hill as described in the snapshot analysis. Comparing with the results shown in Table 1, also highest values of duration ratios are found for sites in these parts of the basin (i.e. stations AE, HU and LC). Remarkably, although we only simulated an aftershock of the sequence following the Maule main shock, the results are quite striking since most of the damages following the 2010 Maule earthquake are concentrated in areas of highest values of the cumulative kinetic energy (Bray & Frost 2010).

However, according to the quality of the input source and the distance of the event, it seems to be not realistic to provide a match in terms of phase arrival, we therefore accomplished a more reliable check by computing the standard spectral ratios (SSR) with respect to the reference station SC, which had been installed on outcropping bedrock, and acceleration response spectra at frequencies from 0.05 to 1.8 Hz. A comparison between the simulated and recorded spectra is shown in Figs 6 and 7.

In general, the curves are in good agreement both for short and long periods. Curves on thick sediments in the northwestern part of the studied area show high amplitudes at lower frequencies. In particular, stations AE in the western and HU in the northern part of the basin show high SSR amplitudes reaching almost 8 and 5, respectively, in agreement with the results of Pilz *et al.* (2009) and the findings described following Fig. 4. On the contrary, the SSRs for most sites in the eastern part of the basin are almost flat with amplitudes around or smaller than 2, indicating only slight amplification. In this part of the basin, a low impedance contrast between the sediments and the underlying bedrock is likely to exist. Furthermore, as expected, stations located on thick sediments (like e.g. AE and CO) also show much smaller soil fundamental resonance frequencies (for the sediment thickness, see Fig. 1), whereas higher fundamental resonance frequencies are found for stations located on thin sediments (like e.g. HU).

The acceleration response spectra in Fig. 7 depict a similar trend, that is, higher amplitudes at lower frequencies for stations located on thick sediments in the northwestern part of the basin, whereas the amplitudes for sites in the eastern part of the basin are generally higher for high frequencies. In agreement with Figs 3 and 6, this might indicate that the vertical variation of the dynamic properties within the sedimentary basin was properly modelled.

On the contrary, only station CO seems to be poorly captured by the simulation, mismatching the fundamental frequency of the soil and underpredicting the observed spectrum. This is also confirmed by the corresponding seismogram in Fig. 3. The mismatch at this site might be due to an improper basin model used in the simulation.

Anyhow, although we have included a complex 3-D basin model in the simulations, considering topography and the shape of the sediment bedrock interface, matching all details of the recorded signals is beyond the scope of this work, also because of the lack of detailed information about the rupture process, upper-crust attenuation parameters and the specific site stratigraphy. The generalized rupture model of this earthquake that has been used incorporates only limited information. Altogether, the discrepancies might be due to the combined effects of a properly characterized seismic source and a more detailed shallow crustal model, including near-surface complex geological irregularities, which often significantly modify ground motion (e.g. Anderson *et al.* 1996). Anyhow, according to the quality of the input data, the agreement obtained seems to be quite satisfactory.

5 SIMULATION OF NEAR-FAULT EARTHQUAKE GROUND MOTION

To further investigate site conditions in the Santiago basin we now focus on a set of parametric analysis considering different locations of possible hypocentres along the San Ramón Fault, a multikilometric frontal thrust at the western front of the Main Cordillera, which

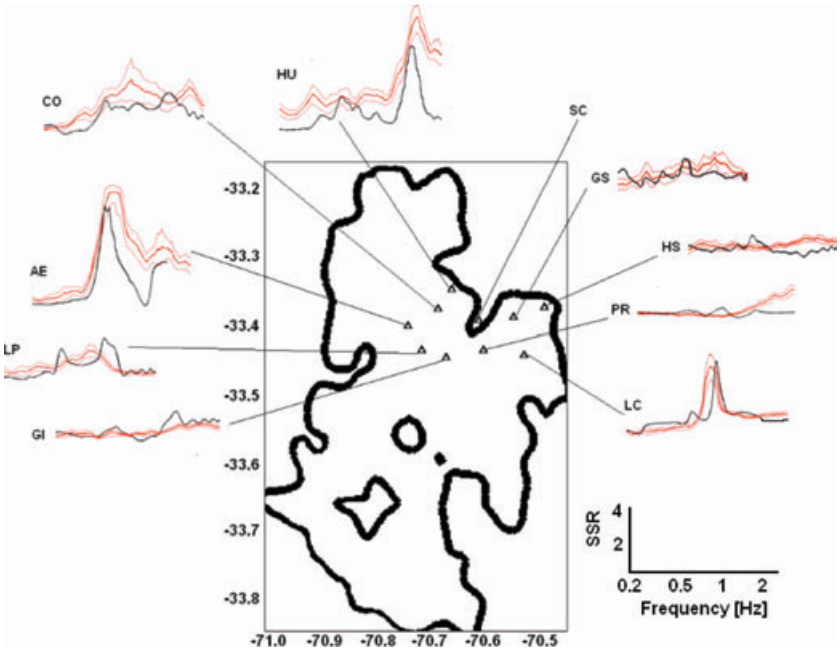

Figure 6. Comparison of standard spectral ratios for recorded (red) and simulated (black) horizontal components for nine sites of the network related to reference station SC. For the recordings, also the standard deviations are shown.

has been shown to pose a significant seismic hazard for the city (Rauld *et al.* 2008; Armijo *et al.* 2010). The best surface expression of the San Ramón Fault is found along an around 15 km long segment with a sharp fault trace in the 25 km long part separating the rivers Mapocho and Maipo along the San Ramón mountain front (see Fig. 1). To this regard, a mesh of the study area has been constructed with similar layering as shown in Fig. 2. The mechanical properties inside the sedimentary basin and the characteristics of the bedrock layers are identical to the ones described above. However, since the San Ramón Fault is located at the edge of the Santiago basin the second model covers only an area of around 86 km × 60 km × 20 km. It consists of 1 483 560 elements with a size ranging from 30 up to 900 metres and the maximum propagated frequency is around 2.5 Hz with a spectral degree 4.

All scenario simulations presented here correspond to earthquakes with a magnitude $M_w = 6.0$ along the central segment of the San Ramón Fault, geometrically defined by a 12 km × 5 km rectangle (Wells & Coppersmith 1994). The parameters of the hypothetic source mechanism (strike = 172°, dip = 119°) are taken from Armijo *et al.* (2010) and are the same for all simulated scenario events. Like before, the rupture is in plane and propagates circularly from one hypocentre with a constant rupture velocity of 2800 m s^{-1}. The slip velocity is around 1 m s^{-1}.

Although a visco-plastic soil model is already implemented in GeoELSE (Di Prisco *et al.* 2007), the large extension of the numerical mesh suggest the use of a simpler non-linear viscoelastic soil model avoiding an excessive increase of computer time. The latter was implemented in GeoELSE as a generalization to 3-D load conditions of the classical G-ε and D-ε curves used within 1-D linear-equivalent approaches (Kramer 1996, Stupazzini *et al.* 2009), where G, D and ε are shear modulus, damping ratio and 1-D shear strain, respectively. For the G-ε and D-ε curves for the non-linear viscoelastic model adopted in this work, standard parameters for shallow clayey soil materials were taken from Seed *et al.* (1986). To extend those curves to the 3-D case, a scalar measure of shear strain amplitude was considered. This implementation allows simulating the non-linear behaviour by means of an iterative process and has been found to converge in a very small number of iterations (2 to 3, Scandella 2007).

In the near-fault zone of an earthquake the directivity effect plays a crucial role (Sommerville *et al.* 1997; Guatteri *et al.* 2003; Stupazzini *et al.* 2009). Combined with the pronounced basin shape and the surface topography, this might result in complex patterns of ground motion. Therefore, we studied this effect taking into account six different hypocentres located along the same fault plane.

Fig. 8 shows the influence of hypocentre location on peak ground velocity (PGV), defined as the square root of the sum of the squares of the velocities for the two horizontal components. We decided to display PGV because this parameter is regarded of being better related to damages that can occur on the top of deep structures like the Santiago basin, since it is representative of the low and intermediate frequency content of the signal (see e.g. Brun *et al.* 2004 and references therein).

In general, for cases in which the earthquake occurs on a fault at the basin margin, as it has already been observed for example, during the Hyogo-ken Nanbu (Kobe) earthquake, the influence of the basin shape becomes very important (e.g. Pitarka *et al.* 1998). As can be seen in Fig. 8 the variability of hypocentre location could trigger PGV values varying of a factor up to 2.5 for the same station. The northeastern part of the basin close to the fault suffers most from the coupling of directivity and basin effects, with the highest PGV values found for all hypocentre locations on the top of a more than 400 m thick sedimentary layer to the southeast of Cerro San Cristóbal. The worst case is hypocentre H1, located relatively shallow at the southern end of the fault, showing PGV values of up to 1.38 m s^{-1}. Also in the northwestern part of the basin, where the sedimentary cover is much thicker (see Fig. 1), considerably higher PGV values (>0.4 m s^{-1}) are found compared to the southwestern part. On the contrary, for hypocentre H6 on the northern end of the fault maximum PGV values are only 0.64 m s^{-1}.

To highlight the influence of the sedimentary basin on seismic wave propagation, Fig. 9 presents snapshots of the velocimetric

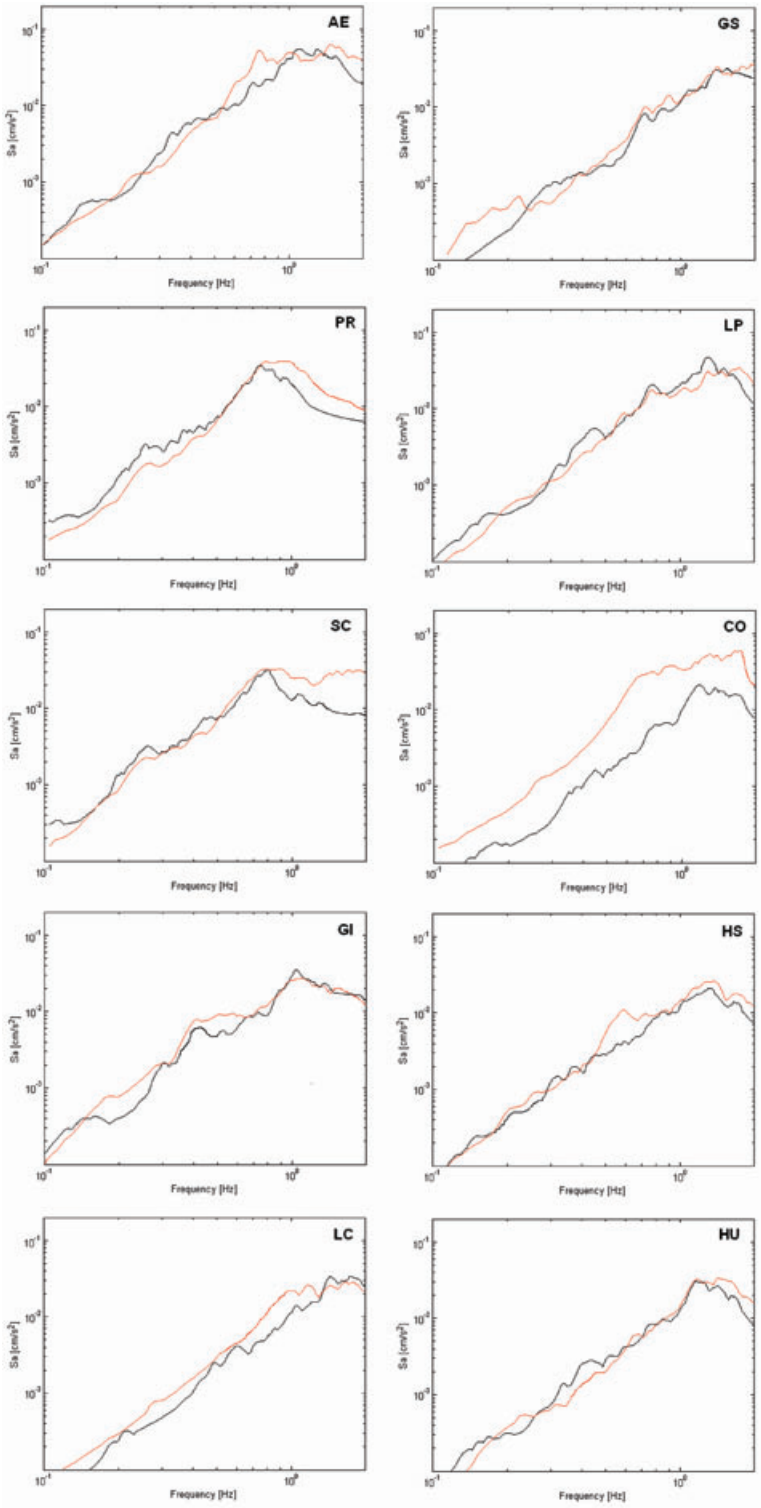

Figure 7. Comparison of the observed 5 per cent-damped acceleration response spectra (red) with the spectra simulated in this study (black) for the vertical component of ground motion for the $M = 5.2$ event on 2010 April 1.

ground motion obtained by the H1 source model. Because the epicentre is located close to the basin edge, source radiation dominates the near field records. However, a clear interaction between the hypocentre location (and the corresponding directivity effects) and the surface topography, in combination with the low wave velocities of the Santiago basin, can be identified. After 6.0 s the rupture propagates radially from the starting point at the eastern basin edge, propagating further into the basin from 9.0 to 12.0 s. Compared to the portion of waves propagating in the western direction, the southwestern and in particular the northwestern wave packets are significantly distorted and are characterized by much larger amplitudes due to the thick sediments. At 13.5 s direct waves propagating

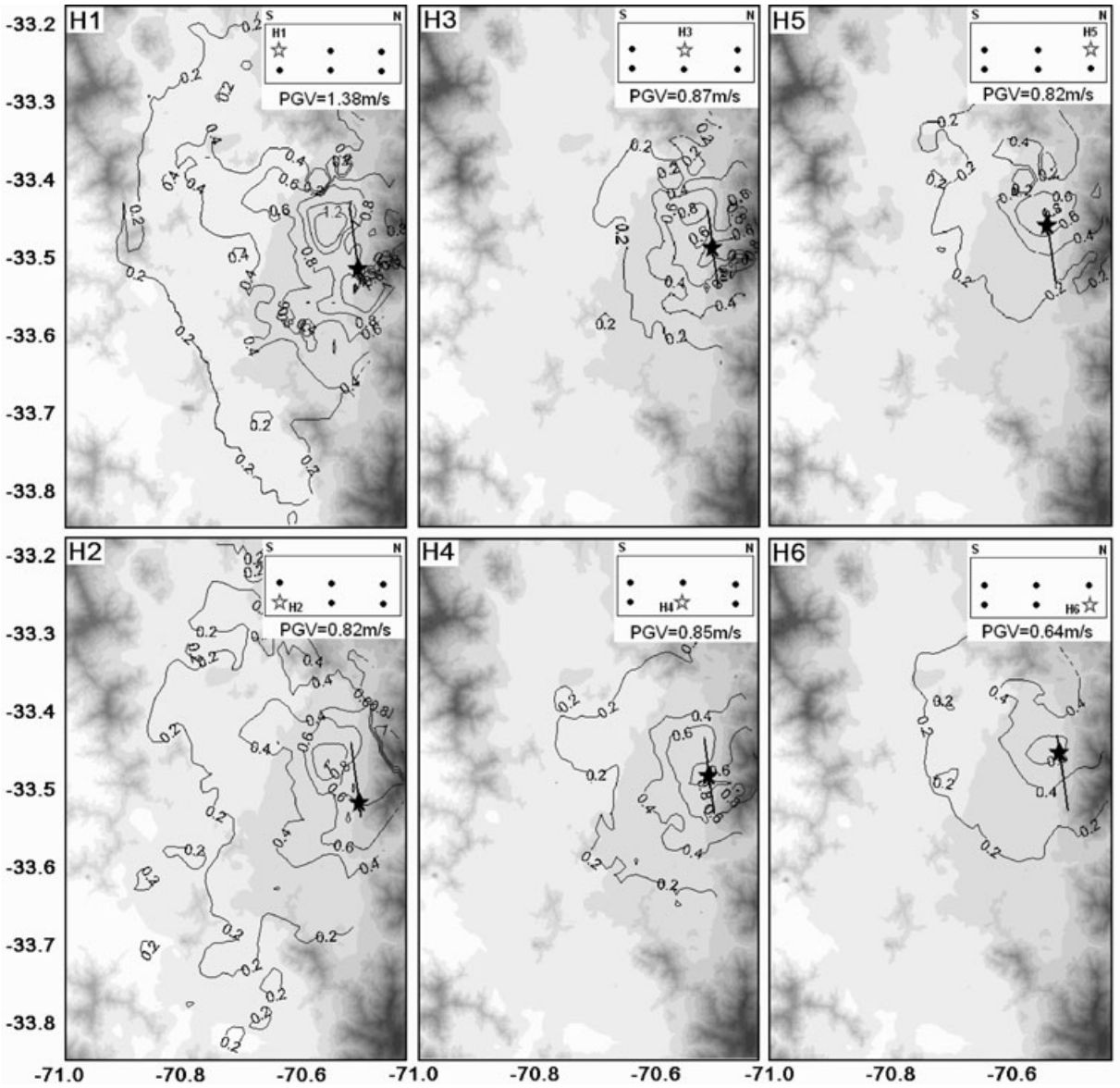

Figure 8. PGV for the various hypocentre locations adopted for the parametric study. Hypocentre locations are indicated by a black star. The thick black line in the east represents the San Ramón Fault. Isoline PGV values are given in metre per second.

toward northwest are reflected at the Cerro San Cristóbal (letter A in Fig. 9), coinciding with later arrivals along a narrow zone to the southeast of the hill. A zone of strong ground motion parallel to the hill can be identified. In general, the width of such amplification zones and their distances from the basin edge depend on several parameters like the frequency content of the incident waves, the exact basin edge geometry, and the velocity contrast between the sediments and the bedrock (e.g. Pitarka *et al.* 1998).

Furthermore, the prograding of waves toward northwest is clearly influenced by the Cerro Renca: low amplitudes are found at the site of the hill (letter B), whereas high amplification is observed southly. Interference effects and trapping of energy at distances of around 15 km from the fault (letter C) can be seen. The ground motion is as large as around 8–10 km west of the fault (letter D). Such trapping effects can also be seen in the waves travelling to the southwest, but they are less significant there.

As can be seen in Fig. 9, complex wave propagation phenomena and a complex PGV distribution pattern are mainly caused topographic and basin effects. To further explicate the effects of high-resolution topography on ground motion, we exemplarily calculate the PGV amplification factor for the scenario simulation with hypocentre H1. To this regard, we subtract the PGV values for the 3-D model taking into account the sedimentary basin shape but without topography from the value for the same basin model including topography, dividing the results by the PGV value for the model without topography. This phenomenon is also addressed by Lee *et al.* (2009). Results are illustrated in Fig. 10.

Outside the basin, in general, surface topography increases PGV values at mountain top, whereas valleys usually have reduced PGV values, that is, a negative amplification factor. From the relative change in PGV it is clear that the PGV amplification is only partially related to the absolute elevation but the variation is mainly controlled by gradients of topography. This is particularly evident near mountain tops where the topographic gradient varies rapidly. As shown in Fig. 10, strong amplification is particularly evident at

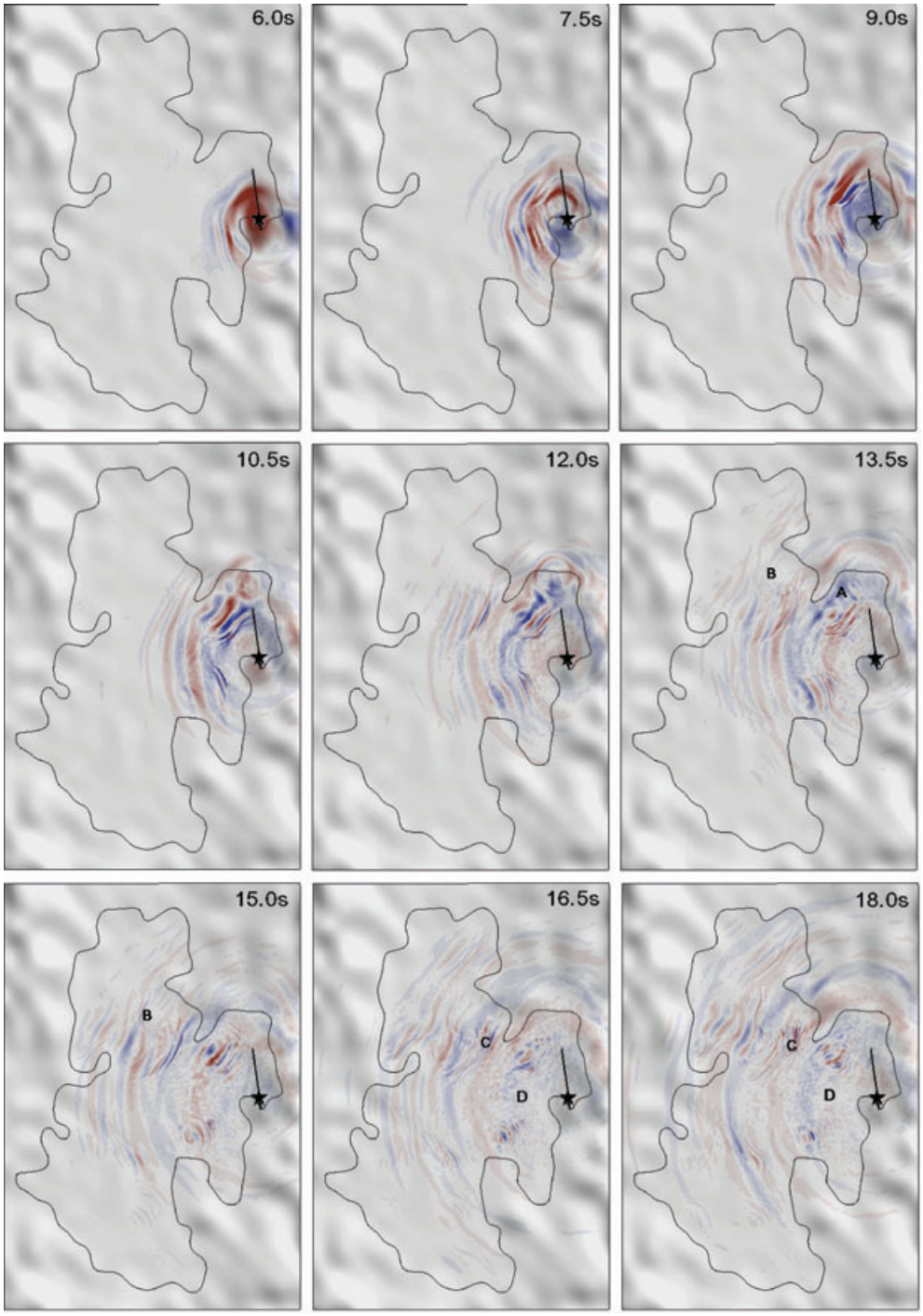

Figure 9. Snapshots of the absolute velocity of the scenario earthquake with hypocentre H1 shown in Fig. 8. Red colours indicate positive velocities and blue colours indicate negative velocities. The black line represents the San Ramón Fault. The adopted hypocentre is indicated by a black star. Letters represents locations discussed in the text.

high mountain ridges in the northeast and southeast of the studied area.

Moreover, also inside the basin the distribution of PGV values becomes considerably more complex when topography is incorporated. It is notable that PGV increases in most parts of the basin when topography is included but effects are especially evident in the western part. Although body waves do not exhibit an apparent change under the influence of topography the high PGV amplification values are likely to be due to the fact that the waves reflect off the western mountain range and, subsequently, propagate back into the basin in a direction almost normal to the basin edge. This results in constructive interference of the wavefields along a narrow zone, thereby significantly increasing the PGV values in this part of the basin. As already described for Fig. 9, this effect can be observed to the southwest of Cerro San Cristóbal (south of letter A in Fig. 9) but is even more evident in a narrow elongated zone in the southwestern part of the basin offset from the basin edge by about 5 km. Although the absolute PGV values rather small, PGV

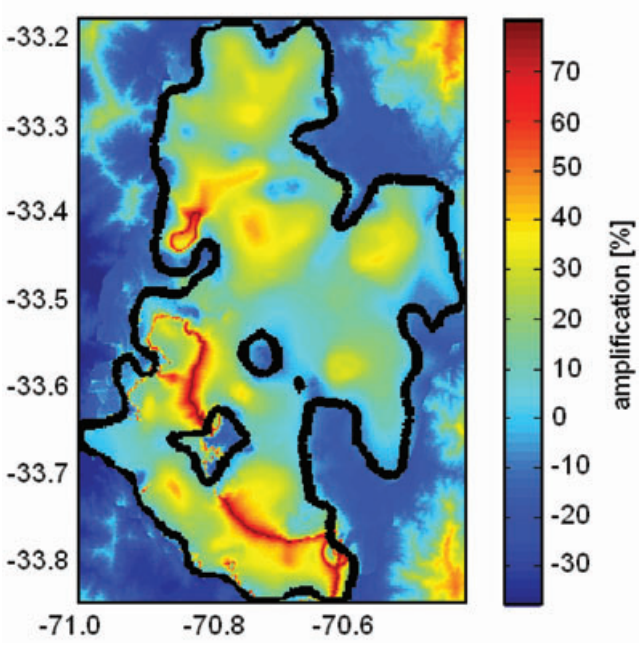

Figure 10. The PGV amplification factor obtained by subtracting the PGV value for the model without topography from the model with topography, dividing the results by the PGV value for the model without topography for the scenario earthquake with hypocentre H1. The black line marks the border between the sedimentary basin and outcropping bedrock.

amplification values higher than 50 per cent can be found here, clearly identifying the basin-edge effect as an important factor influencing ground motion in the Santiago basin and demonstrating the need that high-resolution, realistic topographic features should be taken into account in seismic hazard analysis.

6 DISCUSSION OF THE RESULTS

The results of the simulations point out that (i) the deep alluvial soft-sediment structure, (ii) the radiation mechanism, (iii) the hypocentre location and (iv) the surface topography of the area play a crucial role in near-field ground motion. In particular, the unfavourable interaction between all these parameters may raise concern about large PGV values, or other spectral related quantities, even from low to moderate seismic events.

As shown in Fig. 8, the high variability in PGV very close to the fault found in the simulations implies that exact prediction of ground motion in the near-source region is subject to a high degree of uncertainty and highly event specific. In reality, the specific complexities in the spatial and the temporal variation of the slip distribution on the fault will most likely be different than assumed here. Therefore, the values presented here do not represent an upper bound, in agreement with McGarr & Fletcher (2007), based on Brune (1970) and Ida (1973), who found that the peak slip rate within the near-fault zone of an earthquake does not show any clear and simple scaling with seismic moment or magnitude. Several parameters of the rupture dynamics have not been considered here: the spatial variability of the slip-duration function that tends to be larger around the hypocentre and shortens toward the edges of the fault, with values that depend on the total rupture duration. Heterogeneity in the stress parameters will add additional variability in the typical rise time distribution. Moreover, it is likely that the rise time is also influenced by scale lengths of the slip and stress drop distribution, the local variation of which is substantially smaller than the overall dimensions of the fault. In general, shorter rise times will lead to larger ground motions as the seismic energy is released in a shorter time interval, which is particularly notable at the medium to large distance (Guatteri *et al.* 2003). However, in this study we mainly concentrated on the intermediate to low frequency range, where these differences are expected to have less influence.

Similar arguments also hold for the rupture velocity, which we assumed to be constant. In contrast, irregularities in the rupture velocity have been found to be the predominant source of high-frequency radiation (e.g. Madariaga 1977, Spudich & Frazer 1984). Yet, we assume that this effect might be of limited consequence due to the 2.5 Hz maximum frequency limit considered for the simulations. This limit might also be too low to actually account for strong lateral velocity variations in the sediments and shallow weathered layers in the bedrock. The effect of the detailed shape of the slip velocity function has been found to be less important for the seismic waveforms because the waveforms are determined by the summation of convolved slip functions over the entire fault plane (effectively filtering out small-scale features of the slip-velocity parameterizations, as pointed out by Mai (2009)).

Although we considered non-linear soil behaviour through a non-linear viscoelastic model, its role for the scenario simulations has been found to be less important than source mechanism and hypocentre location since it mainly affects higher frequencies (Yu *et al.* 1993, Beresnev & Wen 1996). The frequency range, in which non-linear deamplification will occur, will significantly depend on the thickness of the soil deposits and might affect the results in our case only marginally. Generally, this effect will appear only in terms of a change in duration of ground motion in the strong motion part of the signal (e.g. Ambraseys *et al.* 2005, Stupazzini *et al.* 2009). Therefore, the major variations of PGV found in this study in the western part of the basin, more distant to the source, are more likely to be related to the arrival later phases (Paolucci & Pitilakis 2007). This can also be seen in Fig. 9 in which, for the southwestern part of the basin, highest amplitudes are generated by later phases.

Moreover, several authors such as Hardin & Drnevich (1972) and Seed *et al.* (1986) have shown the trend of decreasing non-linear behaviour of cohesion less soils with increasing confining pressure. However, the non-linear behaviour of the clayey soils at greater depths in the Santiago basin is difficult to predict. If there is no effect of confining pressure on the behaviour of the clay and since the materials show a high plasticity (Valenzuela 1978), the layers can be supposed to behave non-linearly under dynamic loading, thereby reducing the risk of large shaking amplifications during an earthquake.

Summarizing, although the absolute values shown here are but examples of possible realizations of an earthquake on the San Ramón Fault, the conclusion of this study is that a combination of directivity and basin effects might produce large ground motions in a very dense populated area in the northeastern part of the Santiago basin, where a large part of the city's offices is located, thus largely increasing the seismic risk of that area.

7 COMPARISON WITH EMPIRICAL RELATIONS

Empirical GMPEs attempt to quantify the statistical distribution of ground motion for given magnitude, distance and site conditions. To rank the expected ground motion levels we therefore compare our results with the one predicted by three of such equations, belonging

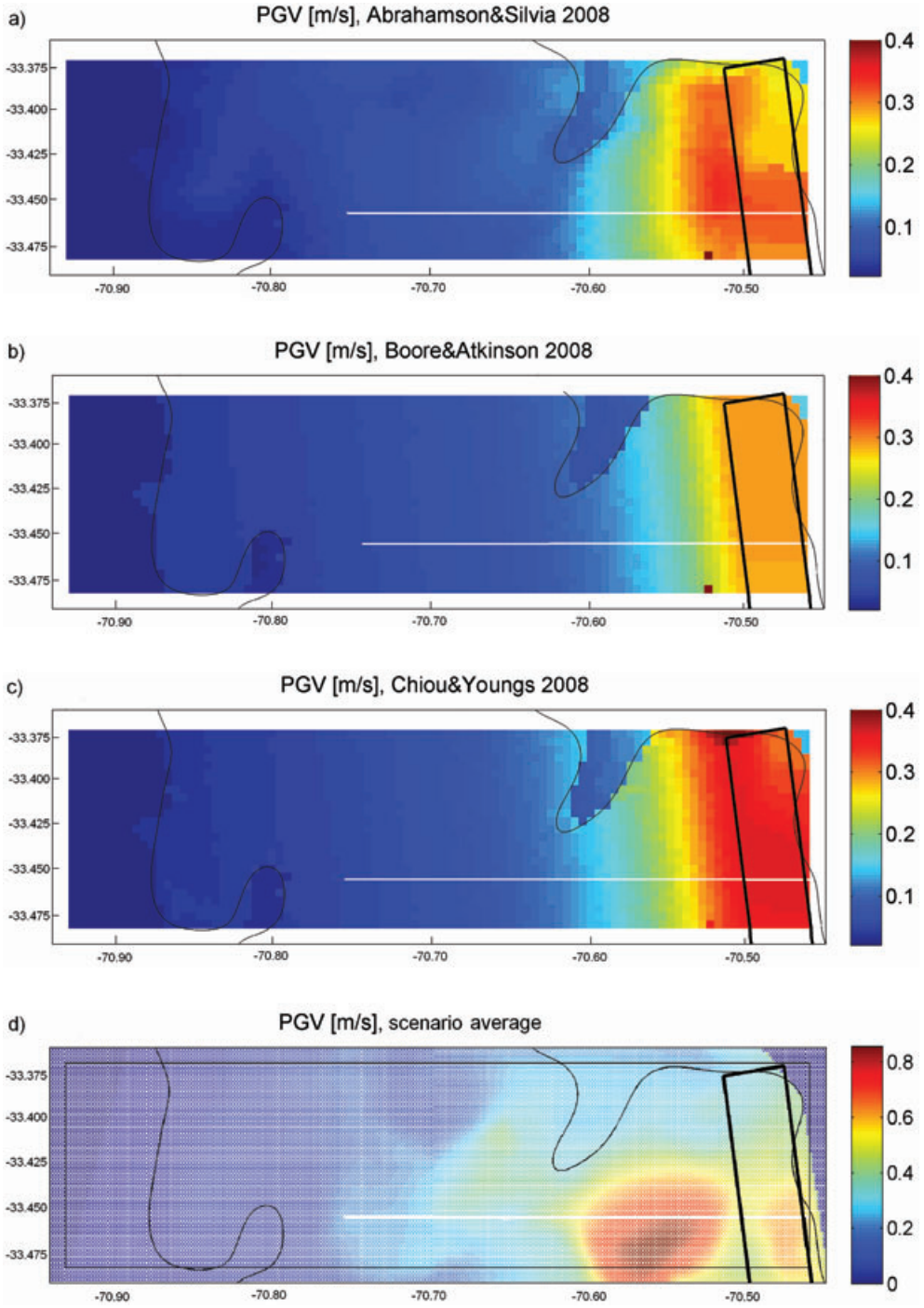

Figure 11. PGV predicted by (a) Abrahamson & Silva (2008), (b) Boore & Atkinson (2008), (c) Chiou & Youngs (2008), (d) GeoELSE averaged over six hypocentre locations shown in Fig. 8. The black rectangle represents the San Ramón Fault. The thin black line marks the border between the sedimentary basin and the outcropping bedrock. The white line indicates cross-sections of PGV shown in Fig. 12. Please note the different amplitude scaling in (d).

to the NGA family, which are based on the same kind of scenario. All considered NGA models use v_s^{30}, the average shear wave velocity in the uppermost 30 m, as a predictor of site effects. Moreover, the relationships provided by Abrahamson & Silva (2008) and by Chiou & Youngs (2008) take into account the effect of the alluvial basin with a specific parameter (Z1) that represents the depth to $v_s = 1000$ m s^{-1}, whereas Boore & Atkinson (2008) neglect any information about thick soft soil deposits.

In Fig. 11 the comparison in terms of PGV is presented. For these comparisons we used the mean of the horizontal component velocity peaks because this is the measure of PGV used in the empirical relationships. Since the three empirical relationships do not take into account any directivity effect we decided to compare their results with the average values obtained with the six different hypocentres shown in Fig. 8. The PGV values agree very well for all three NGA equations, especially more distant from the fault. For

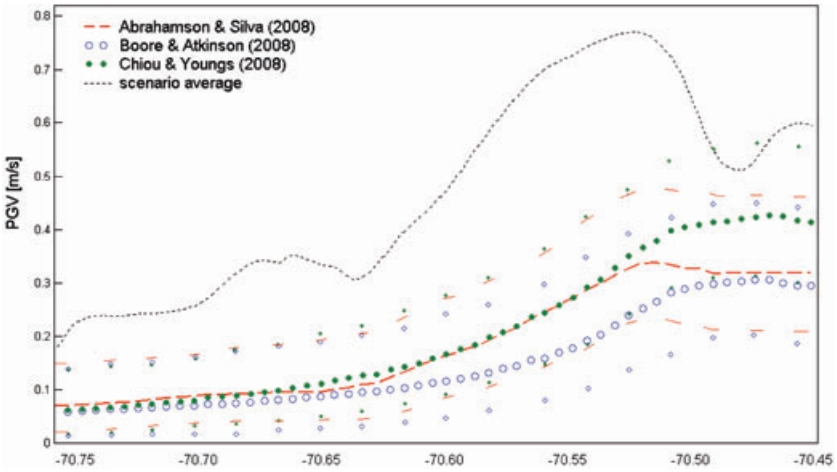

Figure 12. Comparison of PGV cross-sections predicted by Abrahamson & Silva (red line), Boore & Atkinson (blue circles), Chiou & Youngs (green spots) and by GeoELSE averaged over six hypocentre locations. For the NGAs, mean values are shown as thick symbols whereas small symbols represent mean value plus/minus one standard deviation.

all NGAs, the standard deviations are quite large, as expected for the near-fault range and a moderate $M_w = 6.0$ event. Differences in the individual standard deviations result from the treatment of the magnitude dependence and from the influence of non-linear site response on the standard deviation.

Although we averaged only six scenarios clear tendencies can be pointed out. In particular, when comparing with the averaged numerical results with the NGAs, the differences remain dramatic: almost two times higher PGV values are observed and the maximum values of PGV are clearly shifted in the western direction of the alluvial basin (Fig. 12). In particular, whereas PGV values very close to the fault differ only by up to 50 per cent, the highly localized maximum in PGV in Fig. 11(d) and in Fig. 12 for the scenario average, which can also clearly be observed in Fig. 9, appears to reflect the important local effects revealed by the simulations, that is, the channelling of energy into the deep parts of the basin, since the thickness of the sedimentary cover reaches almost 500 m for this part of the basin (see Fig. 1). To a minor degree, this effect can also be observed between longitude 70.70° E and 70.65° E in Fig. 11(d) and Fig. 12, for which the sediment thickness is around 400 m. Although two of the three considered relationships account for a soil/sediment depth factor none of the NGAs is able to capture this effect, that is, the influence of the basin depth.

A comparison of the empirical scenarios with the GeoELSE 3-D deterministic one in terms of response spectral acceleration for 5 per cent damping and a period of $T = 3$ s is shown in Fig. 13. Only the relationship of Abrahamson & Silva (2008) shows a slight influence of the shape of the alluvial basin and produces results which are by trend more similar to the 3-D deterministic modelling. The directivity effect (Rowshandel 2010) is only of minor influence, increasing the maximum Sa by ∼20 per cent [Fig. 13(a) and (b)]. On the other hand, the response spectral acceleration calculated following Chiou & Youngs (2008) seems almost to neglect the influence of the basin shape; the real key parameter is the distance from the fault.

8 CONCLUSIONS

We presented a numerical model of the area surrounding the city of Santiago de Chile, capable of taking into account the superficial geology, the alluvial basin shape and the pronounced surface topography. With a SEM based code, we studied the influence of the surface topography and the basin on seismic wave propagation and could show that the seismic wave pattern is strongly influenced by thick sedimentary cover and its complex interface with the underlying bedrock. The first verification step required a large-scale numerical model of the Santiago basin. The simulation of a regional event, which had been registered by a dense network installed in the city for recording aftershock activity following the 2010 February 27 Maule earthquake, shows that the model, although simplified, is in general capable for realistic calculations of ground motion in terms of amplitude, duration and frequencies up to 1.8 Hz. In particular, the proper implementation of topography and basin shape turns out to play a major role to adequately and quantitatively reproduce the spatial distribution of ground motion within the basin.

We further examined the near-fault earthquake ground motion for a hypothetical event occurring along the active San Ramón Fault, which is crossing the eastern margins of the city. Among the possible factors contributing to ground motion variability, we investigated the role of hypocentre location and corresponding directivity effects, in combination with their coupling with the pronounced topography in the Santiago basin. Within the same location, the peak values of ground velocity were found to vary up to a factor of 2.5, as a function of the position along the fault of the hypocentre. Of course, other source factors like slip velocity and rupture velocity will also significantly influence ground motion but have not been studied here. Although we simplified the complex source dynamic and analysed a limited set of scenarios, our model shows that the unfavourable interaction between fault rupture, radiation mechanism, basin effects and complex topographic conditions may give rise to large values of PGV in the near-field, even for a moment magnitude 6.0 scenario earthquake. Therefore, owing to the available scanty near-fault strong motion data, 3-D numerical simulations presently serve as a valuable tool to provide estimations of near-fault ground motion.

Finally, we compared the results with the NGA predictions, showing a good agreement in the order of magnitude of the simulated quantities far from the fault but differing quite significantly in the spatial distribution of the patches of maximum values. Obviously, results of NGA relationships are mainly driven by the distance from the fault while the 3-D simulations emphasize the crucial role played

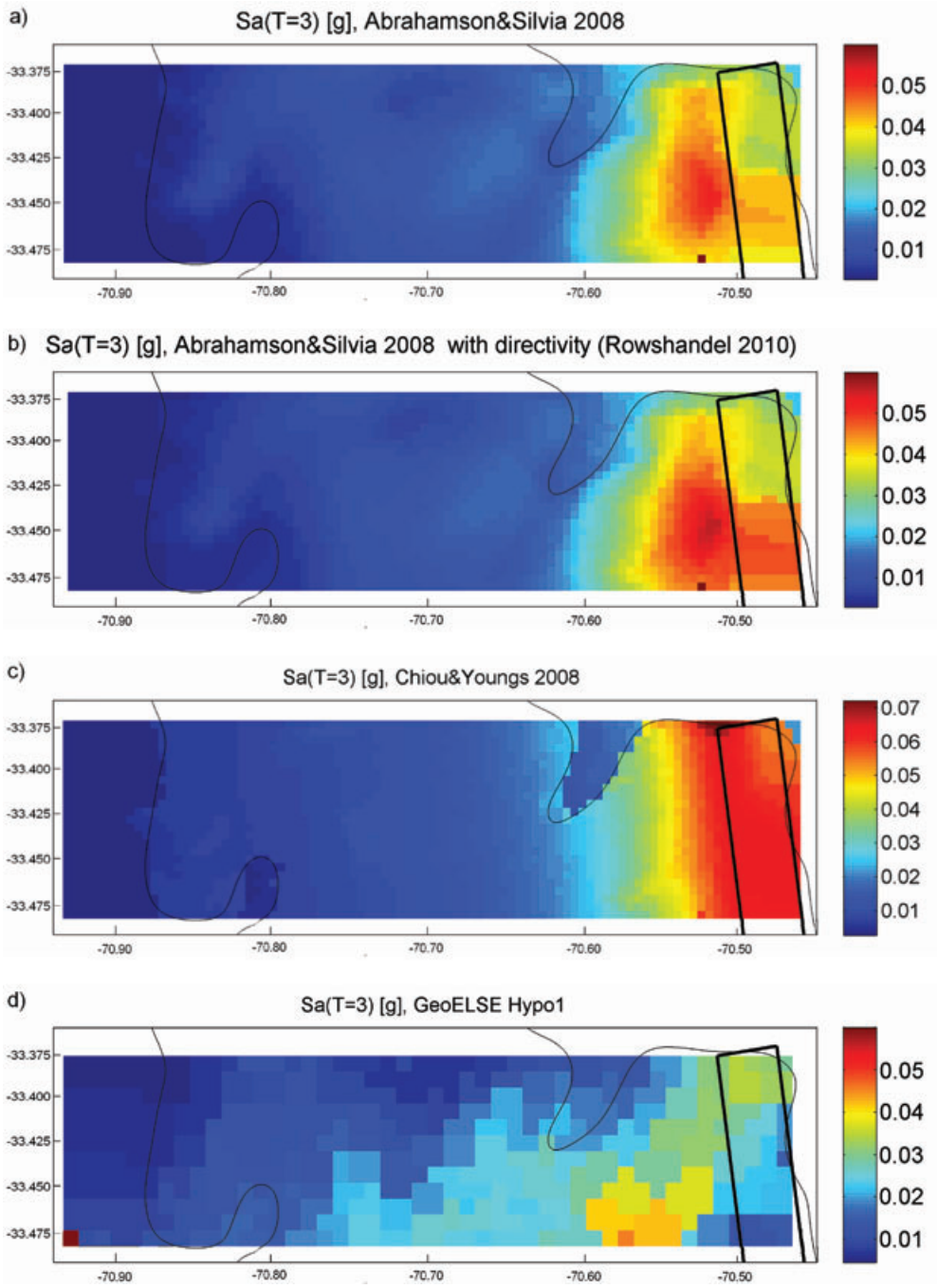

Figure 13. 5 per cent-damped response spectral acceleration Sa (T = 3s) (a) predicted by Abrahamson & Silva (2008), (b) predicted by Abrahamson & Silva (2008) modified for taking into account the directivity effect (Rowshandel 2010), (c) predicted by Chiou & Youngs (2008), (d) predicted by GeoELSE with hypocentre H1. The black rectangle represents the San Ramón Fault. The thin black line marks the edge of the basin.

by the basin shape in determining the PGV map pattern. In particular, all 3-D scenario simulations predict a PGV pattern with highest values concentrated in the most densely populated quarters of the city.

However, although the city of Santiago de Chile basin is very well constrained and also in spite of the computational efforts the numerical prediction of ground motion in general cannot be considered being a mature since it will always exhibit some degree of variability. This is due to both the adopted numerical method but also the structural complexity of the model and the proper definition of the input solicitation. Nevertheless, as concluded by Chaljub *et al.* (2010), despite the geometrical and stratigraphical complexity of sedimentary basins, different numerical methods might provide similar results.

Therefore, it seems reasonable to include 3-D numerical modelling in earthquake hazard assessment since, when used with caution, this techniques are actually able to handle wave radiation phenomena from an extended source and their subsequent propagation in complex 3-D media. The presented results might serve as a basis for this and might also further assist risk reduction programs.

ACKNOWLEDGMENTS

We thank Dimitri Komatitsch and an anonymous reviewer for the thoughtful comments and remarks that significantly improved the quality of the manuscript. We deeply thank CRS4, and in particular F. Maggio and L. Massidda, for the essential cooperation in the development of GeoELSE. Thanks to Chiara Smerzini for helpful discussions and support in figure generation. We also want to acknowledge Erwin Günther and Carolina Honores for assistance during the field work. Kevin Fleming kindly revised our English. The GTOPO30 data set was taken from http://eros.usgs.gov/#/Find_Data/Products_and_Data_Available/gtopo30_info.

REFERENCES

Aagaard, B.T., Hall, J.F., & Heaton, T.H., 2001. Characterization of near-source ground motions with earthquake simulations, *Earthq. Spec.,* **17,** 177–207.

Abrahamson, N.A., & Silva, W.J., 2008. Summary of the Abrahamson and Silva NGA ground motion relations, *Earthq. Spec.,* **24,** 67–97.

Ambraseys, N.N., Douglas, J., Smit, P., & Sarma, S.K., 2005. Equations for the estimation of strong ground motions from shallow crustal earthquakes using data from Europe and the Middle East: horizontal peak ground acceleration and spectral acceleration, *Bull. Earthq. Eng.,* **3,** 1–53.

Anderson, J.G., Lee, Y., Zeng, Y., & Day, S.M., 1996. Control of strong motion by the upper 30 meters, *Bull. seism. Soc. Am.,* **86,** 1749–1759.

Araneda, M., Avendano, F., & Merlo, C., 2000. Gravity model of the basin in Santiago, Stage III, in *9th Chilenian Geological Congress,* Vol. 2, pp. 404–408, Santiago, Chile.

Armijo, R., Rauld, R., Thiele, R., Vargas, G., Campos, J., Lacassin, R., & Kausel, E., 2010. The West Andean Thrust (WAT), the San Ramón Fault and the seismic hazard for Santiago (Chile), *Tectonics,* **29,** TC2007, doi:10.1029/2008TC002427.

Arnold, D.N., 1982. An interior penalty finite element method with discontinuous elements, *SIAM J. Numer. Anal.,* **19,** 742–760.

Bao, H.S., Bielak, J., Ghattas, O., Kallivokas, L., O'Hallaron, D.R., Shewchuk, J.R., & Xu, J.F., 1998. Large-scale simulation of elastic wave propagation in heterogeneous media on parallel computers, *Comput. Meth. appl. Mech. Eng.,* **152,** 85–102.

Barrientos, S., Vera, E., Alvarado, P., & Monfret, T., 2004. Crustal seismicity in central Chile, *J. South Am. Earth Sci.,* **16,** 759–768.

Beresnev, I., & Wen, K., 1996. Nonlinear soil response – a reality? *Bull. seism. Soc. Am.,* **86,** 1964–1978.

Bielak, J., Ghattas, O., & Kim, E.J., 2005. Parallel octree-based finite element method for large-scale earthquake ground motion simulation, *Comput. Model. Eng. Sci.,* **10,** 99–112.

Bindi, D., *et al*., 2009. Site amplifications observed in the gubbio basin, central italy: hints for lateral propagation effects, *Bull. seism. Soc. Am.,* **99,** 741–760.

Blacker, T., *et al*., 1994. *CUBIT Mesh Generation Environment User Manual*, Vol. 1 Sandia National Laboratories, Albuquerque, NM.

Bommer, J.J., & Martínez-Pereira, A. (1999. The effective duration of earthquake strong motion, *J. Earthq. Eng.,* **3,** 127–172.

Boore, D.M., & Atkinson, G.M., 2008. Ground-motion prediction equations for the average horizontal component of PGA, PGV, and 5%-damped PSA at spectral periods between 0.01s and 10.0s, *Earthq. Spec.,* **24,** 99–138.

Bravo, R.D., 1992. Estudio geofisico de los suelos de fundación para un zonificacion sísmica del area urbana de Santiago Norte, *PhD thesis*. Universidad de Chile, Santiago.

Bray, J., & Frost, D., 2010. *Geo-engineering Reconnaissance of the February 27, 2010, Maule, Chile, Earthquake*. Available at: http://www.geerassociation.org/GEER_Post%20EQ%20Reports/Maule_Chile_2010/Cover_Chile_2010.html (last accessed 2010 October 29).

Brun M., Reyouard, J.M., Jezequel, L., & Ile, N., 2004. Damaging potential of low magnitude near-field earthquakes on low-rise shear walls, *Soil Dyn. Earthq. Eng*., **24,** 587–603.

Brune, J.N., 1970. Tectonic stress and the spectra of seismic shear waves from earthquakes, *J. geophys. Res.,* **75,** 4997–5009.

Casarotti E., Stupazzini, M., Lee, S., Komatitsch, D., Piersanti, A., & Tromp, J., 2007. CUBIT and seismic wave propagation based upon the Spectral-Element Method: an advanced unstructured mesher for complex 3D geological media, in *Proceeding of the 16th Int. Meshing Roundtable,* eds Brewer, M.L., & Marcum, D., Springer, New York, NY.

Chaljub, E., Moczo, P., Tsuno, S., Bard, P.Y., Kristek, J., Käser, M., Stupazzini, M., & Kristekova, M., 2010. Quantitative comparison of four numerical predictions of 3D ground motion in the Grenoble Valley, France, *Bull. seism. Soc. Am.,* **100,** 1427–1455.

Chávez-García F.J., & Bard, P.Y., 1994. Site effects in Mexico City eight years after the September 1985 Michoacan earthquakes, *Soil Dyn. Earthq. Eng.,* **135,** 229–247.

Chiou, B., & Youngs, R.R., 2008. Chiou-Youngs NGA ground motion relations for the geometric mean horizontal component of peak and spectral ground motion parameters, *Earthq. Spec.,* **24,** 173–215.

Cockburn, B., Karniadakis, G.E., & Shu, C.W., 2000. The development of discontinuous Galerkin methods, in *Discontinuous Galerkin Methods,* eds Cockburn, B., Karniadakis, G. & Shu, C.W., Springer, Berlin.

Cohen, G., Joly, P., & Tordjman, N., 1993. Construction and analysis of higher-order finite elements with mass lumping for the wave equation, in *Proceedings of the Second International Conference on Mathematical and Numerical Aspects of Wave Propagation,* pp. 152–160, ed Kleinman, R., SIAM, Philadelphia, PA.

Di Prisco, C., Stupazzini, M., & Zambelli, C., 2007. Non-linear SEM numerical analyses of dry dense sand specimens under rapid and dynamic loading, *Int. J. Numer. Anal. Methods Geomech.,* **31,** 757–788.

Dumbser, M., & Käser, M., 2006. An arbitrary high-order discontinuous Galerkin method for elastic waves on unstructured meshes – II. The three-dimensional isotropic case, *Geophys. J. Int.,* **167,** 319–336.

Elnashai, A.S., *et al*. 2010. *The Maule (Chile) Earthquake of February 27, 2010: Consequence Assessment and Case Studies,* MAE Center report 10–04, Urbana, USA.

Faccioli, E., Maggio, F., Paolucci, R., & Quarteroni, A., 1997. 2D and 3D elastic wave propagation by a pseudo-spectral domain decomposition method, *J. Seismol.,* **1,** 237–251.

Falk, R.S., & Richter, G.R., 1999. Explicit finite element methods for symmetric hyperbolic equations, *SIAM J. Numer. Anal.,* **36,** 935–952.

Field, E.H., 1996. Spectral amplification in a sediment-filled valley exhibiting clear basin-edge induced waves, *Bull. seism. Soc. Am.,* **86,** 991–1005.

Frankel, A.D., 1994. Implications of felt area-magnitude relations for earthquake scaling and the average frequency of perceptible ground motion, *Bull. seism. Soc. Am.,* **84,** 462–465.

Frankel, A.D., Carver, D., Cranswick, E., Bice, T., Sell, R., & Hanson, S., 2001. Observations of basin ground motions from a dense seismic array in San Jose, California, *Bull. seism. Soc. Am.,* **91,** 1–12.

Giraldo, F.X., Hesthaven, J.S., & Warburton, T., 2002. Nodal high-order discontinuous Galerkin methods for the spherical shallow water equations, *J. Comp. Phys.,* **181,** 499–525.

Godoy, E., Yañez, G., & Vera, E., 1999. Inversion of an Oligocene volcano-tectonic basin and uplift of its superimposed Miocene magmatic arc, Chilean central Andes: first seismic and gravity evidence, *Tectonophysics,* **306,** 217–326.

Graves, R.W., 1993. Modeling threedimensional site response effects in the Marina District Basin, San Francisco, California, *Bull. seism. Soc. Am.,* **83,** 1042–1063.

Graves, R.W., 1996. Simulating seismic wave propagation in 3D elastic media using staggered grid finite differences, *Bull. seism. Soc. Am.,* **86,** 1091–1106.

Graves, R.W., & Wald, D.J., 2004. Observed and simulated ground motions in the San Bernardino basin region for the Hector Mine, California, earthquake, *Bull. seism. Soc. Am.,* **94,** 131–146.

Guatteri, M., Mai, P.M., Beroza, G.C., & Boatwright, J., 2003. Strong ground motion prediction from stochastic-dynamic source models, *Bull. seism. Soc. Am.,* **93,** 301–313.

Hardin, B.O., & Drnevich, V.P., 1972. Shear modulus and damping in soils: measurement and parameter effects, *J. Soil Mech. Found. Div., ASCE,* **98,** 603–624.

Harmsen, S., Hartzell, S., & Liu, P., 2008. Simulated ground motion in Santa Clara Valley, California, and vicinity from M 6.7 scenario earthquakes, *Bull. seism. Soc. Am.,* **98,** 1243–1271.

Hartzell, S., *et al*., 2006. Modeling and validation of a 3D velocity structure for the Santa Clara Valley, California, for seismic wave simulations, *Bull. seism. Soc. Am.,* **96,** 1851–1881.

Hatayama, K., Matsunami, K., Iwata, T., & Irikura, K., 1995. Basin-induced Love waves in the eastern part of the Osaka Basin, *J. Phys. Earth,* **43,** 131–155.

Hisada, Y., Aki, K., & Teng, T.L., 1993. 3-D simulations of surface wave propagation in the Kanto sedimentary basin, Japan. Part 2: application of the surface wave BEM, *Bull. seism. Soc. Am.,* **83,** 1700–1720.

Horike, M., Uebayashi, H., & Takeuchi, Y., 1990. Seismic response in three-dimensional sedimentary basin due to plane S-wave incidence, *J. Phys. Earth,* **38,** 261–284.

Hu, F.Q., Hussaini, M.Y., & Rasetarinera, P., 1999. An analysis of the discontinuous Galerkin method for wave propagation problems, *J. Comput. Phys.,* **151,** 921–946.

Ida, Y., 1973. The maximum acceleration of strong ground motion, *Bull. seism. Soc. Am.,* **63,** 959–968.

Kagawa, T., Sawada, S., & Iwasaki, Y., 1992. On the relationship between azimuth dependency of earthquake ground motion and deep basin structure beneath the Osaka Plain, *J. Phys. Earth,* **40,** 73–83.

Käser, M., & Dumbser, M., 2006. An arbitrary high-order discontinuous Galerkin method for elastic waves on unstructured meshes – I. The two-dimensional isotropic case with external source terms, *Geophys. J. Int.,* **166,** 855–877.

Kinoshita, S., Fujiwara, H., Mikoshiba, T., & Hoshino, T., 1992. Secondary Love waves observed by a strong motion array in the Tokyo lowlands, Japan, *J. Phys. Earth,* **40,** 99–116.

Kitsunezaki, C., *et al*., 1990. Estimation of P- and S-wave velocities in deep soil deposits for evaluating ground vibrations in earthquake, *J. Jap. Soc. Nat. Disaster Sci.,* **9,** 1–17.

Komatitsch, D., 1997. Méthodes spectrales et éléments spectraux pour l'équation de l'élastodynamique 2D et 3D en milieu hétérogène, *PhD thesis,* Institut de Physique du Globe de Paris (in French).

Komatitsch, D., & Vilotte, J.P., 1998. The spectral-element method: an efficient tool to simulate the seismic response of 2D and 3D geological structures, *Bull. seism. Soc. Am.,* **88,** 368–392.

Komatitsch, D., Vilotte, J.P., Vai, R., Castillo-Covarrubias, J.M., & Sanchez-Sesma, F.J., 1999. The spectral element method for elastic wave equations. Application to 2D and 3D seismic problems, *Int. J. Numer. Meth. Eng.,* **45,** 1139–1164.

Kosloff, R., & Kosloff, D., 1986. Absorbing boundaries for wave propagation problems, *J. Comp. Phys.,* **63,** 363–376.

Kramer, S.L., 1996. *Geotechnical Earthquake Engineering,* Prentice Hall, New York, USA.

Lee, S.J., Chen, H.W., Liu, Q., Komatitsch, D., Huang, B.S., & Tromp, J., 2008a. Three-dimensional simulations of seismic wave propagation in the Taipei basin with realistic topography based upon the spectral-element method, *Bull. seism. Soc. Am.,* **98,** 253–264.

Lee, S.J., Chen, H.W., & Huang, B.S., 2008b. Simulations of strong ground motion and 3D amplification effect in the Taipei Basin by using a composite grid finite-difference method, *Bull. seism. Soc. Am.,* **98,** 1229–1242.

Lee, S.J., Komatitsch, D., Huang, B.S., & Tromp, J., 2009. Effects of topography on seismic wave propagation: an example from Northern Taiwan, *Bull. seism. Soc. Am.,* **99,** 314–325.

Madariaga, R., 1977. High-frequency radiation from crack (stress drop) models of earthquake faulting, *Geophys. J. R. astr. Soc.,* **51,** 625–651.

Mai, P.M., 2009. Ground-motion complexity and scaling in the near-field of earthquake ruptures, in *Encyclopedia of Complexity and System Sciences,* pp. 4435–4474, ed. Meyers, R., Springer, Berlin.

McGarr A., & Fletcher, J.B., 2007. Near-fault peak ground velocity from earthquake and laboratory data, *Bull. seism. Soc. Am.,* **97,** 1502–1510.

Mitchell, S., 1996. A characterization of the quadrilateral meshes of a surface which admit a compatible hexahedral mesh of the enclosed volume, in *Lecture Notes in Computer Science,* eds Puech, C. & Reischuk, R., *STACS 96*, **1046,** Springer, Berlin.

Moczo, P., Lucká, M., Kristek, J. & Kristekové, M., 1999. 3D displacement finite differences and a combined memory optimization, *Bull. seism. Soc. Am.,* **89,** 69–79.

Moczo, P., Kristek, J., Vavrycuk, V., Archuleta, R.J., & Halada, L., 2002. 3D heterogeneous staggered-grid finite-difference modeling of seismic motion with volume harmonic and arithmetic averaging of elastic moduli and densities, *Bull. seism. Soc. Am.,* **92,** 3042–3066.

Olsen, K.B., Archuleta, R., & Matarese, J., 1995. Magnitude 7.75 earthquake on the San Andreas fault: three-dimensional ground motion in Los Angeles, *Science,* **270,** 1628–1632.

Olsen, K.B., Pechmann, J.C., & Schuster, G.T., 1996. An analysis of simulated and observed blast records in the Salt Lake basin, *Bull. seism. Soc. Am.,* **86,** 1061–1076.

Olsen, K.B., *et al*., 2006. Strong shaking in Los Angeles expected from southern San Andreas earthquake, *Geophys. Res. Lett.,* **33,** L07305, doi:10.1029/2005GL025472.

Paolucci, R., & Pitilakis, K., 2007. Seismic risk assessment of underground structures under transient ground deformations, in: *Earthquake Geotechnical Engineering,* pp. 433–459, ed. Pitilakis, K., Springer, Berlin.

Patera, A.T., 1984. A spectral element method for fluid dynamics: laminar flow in a channel expansion, *J. Comput. Phys.,* **54,** 468–488.

Peter, D., *et al*., 2011. Forward and adjoint simulations of seismic wave propagation on fully unstructured hexahedral meshes, *Geophys. J. Int.,* **186,** 721–739, doi:10.1111/j.1365-246X.2011.05044.x.

Phillips, W.S., Kinoshita, S., & Fujiwara, H., 1993. Basin-induced Love waves observed using the strong-motion array at Fuchu, Japan, *Bull. seism. Soc. Am.,* **83,** 64–84.

Pilz, M., Parolai, S., Leyton, F., Campos, J., & Zschau, J., 2009. A comparison of site response techniques using earthquake data and ambient seismic noise analysis in the large urban area of Santiago de Chile, *Geophys. J. Int.,* **178,** 713–728.

Pilz, M., Parolai, S., Picozzi, M., Wang, R., Leyton, F., Campos, J., & Zschau, J., 2010. Shear wave velocity model of the Santiago de Chile basin derived from ambient noise measurements: a comparison of proxies for seismic site conditions and amplification, *Geophys. J. Int.,* **182,** 355–367.

Pilz, M., Parolai, S., Picozzi, M., & Zschau, J., 2011. Evaluation of proxies for seismic site conditions in large urban areas: The example of Santiago de Chile, *J. Phys. Chem. Earth,* doi:10.1016/j.pce.2011.01.007.

Pitarka, A., Irikura, K., Iwata, T., & Sekiguchi, H., 1998. Three-dimensional simulation of the near-fault ground motion for the 1995 Hyogoken Nanbu (Kobe), Japan, earthquake, *Bull. seism. Soc. Am.,* **88,** 428–440.

Priolo, E., Carcione, J.M., & Seriani, G., 1994. Numerical simulation of interface waves by high-order spectral modeling techniques, *J. acoust. Soc. Am.,* **95,** 681–693.

Rauld, R., Armijo, R., Vargas, G., & Thiele, R., 2008. Morphology, geometry and kinematics of the San Ramón fault crossing Santiago, Chile (33.5° S), in *4th Alexander von Humboldt International Conference – The Andes: Challenge for geosciences,* Santiago, Chile, paper 212.

Reed, W.H., & Hill, T.R., 1973. Triangular mesh methods for the neutron transport equation, Technical Report, LA-UR-73–479, Los Alamos Scientific Laboratory.

Rivière, B., & Wheeler, M.F., 2003. A posteriori error estimates for a discontinuous Galerkin method applied to ellipcitc problems, *Comput. Math. Appl.,* **46,** 141–163.

Seed H.B., Wong, R.T., Idriss, I.M., & Tokimatsu, K., 1986. Moduli and damping factors for dynamic analyses of cohesionless soils, *J. Geotech. Eng. ASCE,* **112,** 1016–1032.

Rowshandel, B., 2010. Directivity corrections for the Next Generation Attenuation (NGA) relations, *Earthq. Spec.,* **26,** 525–559.

Scandella, L., 2007. Numerical Evaluation of Transient Ground strains for the seismic response analisys of underground structures, *PhD thesis*. Politecnico di Milano, Italy.

Seriani, G., & Priolo, E., 1994. A spectral element method for acoustic wave simulation in heterogeneous media, *Finite Elem. Anal. Des.,* **16,** 337–348.

Seriani, G., Priolo, E., & Pregarz, A., 1995. Modelling waves in anisotropic media by a spectral element method, in *Proceedings of the Third International Conference on Mathematical and Numerical Aspects of Wave Propagation,* pp. 289–298, ed Cohen, G., SIAM, Philadephia, PA.

Sommerville, P.G., Smith, N.F., Graves, R.W., & Abrahamson, N.A., 1997. Modification of empirical strong ground motion attenuation relations to include the amplitude and duration effects of rupture directivity, *Seismol. Res. Lett.,* **68,** 199–222.

Spudich, P., & Frazer, L.N., 1984. Use of ray theory to calculate high frequency radiation from earhquake sources having spatially variable rupture velocity and stress drop, *Bull. seism. Soc. Am.,* **74,** 2061–2082.

Stupazzini M., Paolucci, R., & Igel, H., 2009. Near-fault earthquake ground motion simulation in the Grenoble valley by a high-performance spectral element code, *Bull. seism. Soc. Am.,* **99,** 286–301.

Trifunac, M.D., & Brady, A.G., 1975. A study on the duration of strong earthquake ground motion, *Bull. seism. Soc. Am.,* **65,** 581–626.

Valenzuela, G.B., 1978. Suelo de fundación del Gran Santiago, *Inst. Invest. Geol. Santiago, Chile, Bol*., **33,** 1–27.

Wells, D., & Coppersmith, K., 1994. New empirical relationships among magnitude, rupture length, rupture width, rupture area, and surface displacement, *Bull. seism. Soc. Am.,* **84,** 974–1002.

White, D.R., Mingwu, L., Benzley, S.E., & Sjaardema, G.D., 1995. Automated hexahedral mesh generation by virtual decomposition, in *Proceedings of the 4th International Meshing Roundtable,* Albuquerque, NM, pp. 165–176.

Yu, G., Anderson, J.G., & Siddharthan, R., 1993. On the characteristics of nonlinear soil response, *Bull. seism. Soc. Am.,* **83,** 218–244.